Numerical Analysis and Data Comparison of a Supercritical Water Oxidation Reactor

Chang H. Oh, Robert J. Kochan, and John M. Beller
Idaho National Engineering and Environmental Laboratory, Lockheed Martin Idaho Technologies Company, Idaho Falls, ID 83415

Supercritical water oxidation of isopropyl alcohol was investigated in a pilot-scale reactor. A computational fluid-dynamics model developed reveals the detailed flow field, chemical-component distribution, temperature distribution, and salt-particle trajectories in the reactor flow domain. The near-wall fluid temperature from the numerical analysis was compared with experimental temperature data. The temperature comparison was within a 3% error band. The effect of the chemical kinetic rate was investigated for four different rates. Turbulent salt-particle trajectories were also calculated to investigate the effect of particle sizes on salt deposit on the wall. Also, a method of calculating the adiabatic reaction temperature was developed to estimate reaction temperatures prior to a full numerical simulation.

Introduction

The oxidation of a variety of chemical contaminants in supercritical water has been recently reported (Tester et al., 1992; Savage et al., 1995). The process is based on bringing water, organics, and oxygen together at conditions above the critical point of water (374°C, 221 bar). Under these conditions organics are rapidly oxidized to carbon dioxide and water (Modell, 1989). The technology is currently being investigated by numerous government organizations (Kochan and Oh, 1995; Moore and Simonson, 1993; Rice et al., 1993; Buelow et al., 1990), universities (Savage and Smith, 1995; Tester et al., 1993; Gloyna, 1989; Johnston and Haynes, 1987; Klein et al., 1990, Dixon and Abraham, 1992; Brennecke and Eckert, 1989), and private industry (Modell, 1985; Killilea et al., 1992; Barner et al., 1992; McBrayer and Griffith, 1995) as a non-polluting alternative to other waste-disposal techniques such as incineration and biological treatment.

The solvation properties of supercritical water (Cummings and Chialvo, 1994) are significantly different from liquid water and steam. Liquid water at ambient temperatures has a dielectric constant of approximately 80, due largely to hydrogen bonding. As the temperature is increased, the dielectric constant of water decreases. Above its critical point, the hydrogen bonding between water molecules is very small. The dielectric constant of water (Uematsu and Frank, 1980) and the ionic dissociation constant (Marshall and Franck, 1981) under these conditions is on the order of 1 to 10 and approximately -20 $(mol/kg)^2$, respectively. This results in supercritical water being an excellent solvent for most organic compounds. These unique solvation characteristics of supercritical water makes chemical oxidation very rapid and complete, which results in high destruction efficiencies.

In addition, most inorganic salts exhibit sharply reduced solubilities above the critical point and will rapidly precipitate out of solution. These physical and chemical characteristics led to the development of the vertical reactor process wherein hazardous wastes are oxidized and inorganic salts are separated in a single reactor vessel. Inorganic salts created by feed neutralization, as well as salts present in the initial waste feed stream, precipitate in the reaction medium due to the low solubility in the supercritical water, and can be dissolved in a cold liquid pool at the bottom of MODAR's vertical vessel, to be separated out of the reactor. The process has demonstrated high destruction efficiencies of hazardous organic constituents in excess of 99.99% in a single step (Hong, 1995). The relatively low temperature (less than 600°C) process precludes the formation of primary pollutants, NO_x and SO_2.

SCWO Reactor Configuration

The MODAR supercritical water oxidation (SCWO) pilot scale reactor is a vertical-vessel-type reactor. The reactor consists of a vertical vessel, a coaxial nozzle, and a conical bottom portion where salts formed by neutralization are separated, as shown in Figure 1. The nozzle design and configuration is the most important configuration in the reactor. It

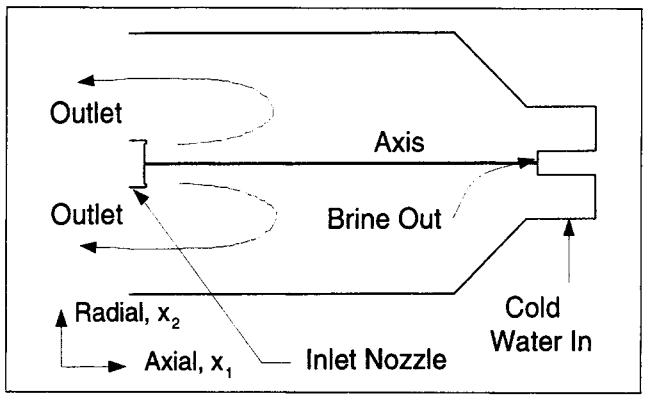

Figure 1. MODAR pilot-scale SCWO vessel reactor.

feeds chemical constituents and oxygen to the reactor. Depending on the nozzle design, it can minimize salt deposits along the wall through its influence on the salt-particle transport in the reactor. The percentage of organics in the feed stream determines the exothermic energy release in the chemical reaction, which eventually determines the temperature in the reactor flow domain. The typical throughput is 4.4×10^6 J/kg heating value in the waste feed stream (Oh and Kochan, 1995). This heating value maintains the reactor temperature at about 600°C. Since the reactor is operated at high pressures, the heating value of 4.4×10^6 J/kg becomes a reactor design constraint, because a higher heating value requires a thicker reactor pressure vessel. This is not desirable in terms of reactor safety and construction cost.

A brine pool is provided at the bottom of the reactor where the precipitated salt is dissolved and separated through the exit pipe. Cold water is fed to the brine pool to maintain the pool level.

Numerical Procedure

Governing equations

This problem consists of three-dimensional turbulent (Reynolds number downstream of the nozzle is 300,000) flow in the vertical-vessel reactor. In these calculations, an assumption of two-dimensional flow is used because of the axisymmetricity of the reactor geometry.

The flow field in the reactor is described by the mass, momentum, and energy-conservation equations:

$$\frac{\partial \rho}{\partial t}+\frac{\partial}{\partial x_i}(\rho u_i)=\dot{m}'' \tag{1}$$

$$\frac{\partial}{\partial t}(\rho u_i)+\frac{\partial}{\partial x_j}(\rho u_i u_j)=-\frac{\partial P}{\partial x_i}+\frac{\partial}{\partial x_j}\left[\mu\left(\frac{\partial u_i}{\partial x_j}+\frac{\partial u_j}{\partial x_i}\right)\right]+\rho g_i+F_i \tag{2}$$

$$\frac{\partial(\rho h)}{\partial t}+\frac{\partial}{\partial x_i}(\rho u_i h)=\frac{\partial}{\partial x_i}\left(k\frac{\partial T}{\partial x_i}\right)-\frac{\partial}{\partial x_i}\sum_{j'}h_{j'}J_{j'}+\frac{DP}{Dt}+\tau_{ij}\frac{\partial u_i}{\partial x_j}+S_h, \tag{3}$$

where x_i is the distance in the ith direction; u_i is the fluid velocity component; ρ is the fluid density; $\dot{m}''$ is the rate of mass addition to the fluid; P is the static pressure; μ is the dynamic viscosity of the fluid; g_i is the gravitational acceleration; F_i are external body forces; h is the static enthalpy; k is the molecular conductivity; k_t is the turbulent conductivity; $J_{j'}$ is the flux of species j'; τ_{ij} is the viscous stress tensor; and S_h is a source term that includes the heat of chemical reaction. The numerical solution of the governing partial differential equations (Eqs. 1–3) begins with discretization of the field into a collection of control volumes. The differential equations are approximated by a set of algebraic equations on this collection, and this system of algebraic equations is then solved to produce a set of discrete values that approximate the solution of the partial differential system over the field. First, it is realized that the governing equations can be rewritten in a canonical form (Patankar, 1980) as

$$\frac{\partial}{\partial x_i}(\rho u_i\phi)=\frac{\partial}{\partial x_i}\left(\Gamma\frac{\partial\phi}{\partial x_i}\right)+S, \tag{4}$$

where the generic dependent variable ϕ, diffusion coefficient Γ, and source term S can be specified to uniquely define a particular equation. In this study, the algebraic equation system is solved by the algorithm called SIMPLE (Patankar, 1980), a semiimplicit iterative scheme that starts from an initial guess and converges to the correct solution after performing a sufficient number of iterations.

The numerical techniques described thus far are available from several commercial computational fluid dynamics software packages (e.g., Fluent, 1996). The effective viscosity is defined by the relation

$$\mu_{\text{eff}}=\mu+\mu_t, \tag{5}$$

where μ is the molecular viscosity and μ_t is the turbulent viscosity deduced by employing a turbulence model. In this study, the renormalization group (RNG) k-ϵ turbulence model (Yakhot and Orszag, 1986) is used. The RNG-based k-ϵ turbulence model follows the two-equation turbulence modeling framework and uses dynamic scaling and invariance together with iterated perturbation methods. The transport equations for the turbulent kinetic energy, k, and the turbulent dissipation, ϵ, in the RNG model are

$$\frac{\partial k}{\partial t}+u_i\frac{\partial k}{\partial x_i}=\mu_t S^2-\epsilon+\frac{\partial}{\partial x_i}\left(\alpha\mu_t\frac{\partial k}{\partial x_i}\right) \tag{6}$$

$$\frac{\partial \epsilon}{\partial t}+u_i\frac{\partial \epsilon}{\partial x_i}=C_1\frac{\epsilon}{k}\mu_t S^2-C_2\frac{\epsilon^2}{k}+\frac{\partial}{\partial x_i}\left(\alpha\mu_t\frac{\partial \epsilon}{\partial x_i}\right)-R, \tag{7}$$

where $S^2=2S_{ij}S_{ij}$ is the modulus of the rate of strain tensor, C_1 and C_2 are 1.42 and 1.68, respectively, α is 1.39, and

$$R=\frac{0.09\eta^3(1-\eta/\eta_o)}{1+\beta\eta^3}\frac{\partial\epsilon^2}{k},$$

where $\eta=Sk/\epsilon$, $\eta_o=4.38$, and $\beta=0.012$. The study performed by Orszag et al. (1993) indicates that the RNG k-ϵ

turbulence model is more accurate than the standard k-ϵ turbulence model, particularly for the flow recirculation and vortex shedding situation.

The conservation of species j' is described by the following equation:

$$\frac{\partial}{\partial t}(\rho m_{j'}) + \frac{\partial}{\partial x_i}(\rho u_i m_{j'}) = \frac{\partial}{\partial x_i}(J_{j',i}) + S_{j'}, \quad (8)$$

where $m_{j'}$ is the mass fraction of species j', $J_{j',i}$ is the diffusive mass flux of species j' in the ith direction, and $S_{j'}$ is the net rate of production of species j' per unit volume due to chemical reaction.

Calculations were performed using a single-step chemical reaction model that was either diffusion-controlled or kinetically controlled. For the kinetically controlled model, an Arrhenius expression was used to calculate the reaction rate, and for the diffusion-controlled model, the turbulence levels were used. It was assumed that the minimum of the two rates controls the reaction.

The eddy breakup model of Magnussen and Hjertager (1976) is used to model the effect of turbulence on the reaction rate:

$$R_{\text{eddy}} = -\frac{d[C_3H_7OH]}{dt} = 4 * \min\left(\frac{M_{O_2} * MW_{C_3H_7OH}}{4.5 * MW_{O_2}}, M_{C_3H_7OH}\right)\frac{\rho\epsilon}{k}, \quad (9)$$

where M and MW are the mass fraction and molecular weight, respectively.

The trajectory of a dispersed particle was obtained by integrating the force balance on the particle, which is in a Lagrangian fashion. This method equates the particle inertia with the forces acting on the particle as shown below:

$$\frac{du_p}{dt} = F_D(u - u_p) + g(\rho_p - \rho)/\rho_p, \quad (10)$$

where $F_D(u - u_p)$ is the drag force per unit particle mass, u is the fluid-phase velocity, u_p is the particle velocity, and

$$F_D = \frac{18\mu}{\rho_p D_p^2}\frac{C_D Re}{24}, \quad (11)$$

where C_D is the drag coefficient and a function of the relative Reynolds number of the following general form:

$$C_D = a_1 + a_2/Re + a_3/Re^2, \quad (12)$$

where the a's are constants that apply over several ranges of Re given by Morsi and Alexander (1972).

Boundary conditions

The geometry is symmetried with respect to the vessel axis center line. At the symmetry boundary, the normal velocity and normal gradients of all variables are zero:

$$\frac{\partial u_1}{\partial x_2} = 0, \qquad \frac{\partial u_2}{\partial x_1} = 0. \quad (13)$$

The MODAR proprietary vessel reactor is shown earlier in Figure 1. This figure is not to scale; the actual reactor length is proportionally greater than shown. The domain was discretized into 209 axial × 35 radial (7,315 total) cells representing axisymetrically one-half of the reactor. The thin oxidant inlet nozzle annulus was modeled by a single cell, while the larger waste inlet inner or core nozzle flow was modeled by five cells. The proprietary nozzle injects oxidant, waste, and supercritical water vertically downward. The boundary conditions of the vessel reactor computational domain include:

1. A coaxial inlet nozzle introducing 1.18 kg/min of water and 0.125 kg/min of isopropyl alcohol in the core at 234.4 bar and 50°C. The annular flow in the nozzle consists of 1.539 kg/min of air and 1.305 kg/min water at 234.4 bar and 620°C. A uniform axial velocity profile was assumed at the core and annular nozzle exit.
2. Flow exits at the upper section.
3. An axisymmetric boundary condition along the vessel center line.
4. The reactor was insulated from the top head down to the conical section with approximately 3 in. of vermiculite to reduce the heat losses. A heat-transfer coefficient of 1.96 $W/m^2 \cdot K$ and an effective ambient temperature of 27°C were used to simulate these conditions.
5. The conical section and the bottom cylinder were uninsulated. For the simulation a linear wall-temperature distribution was assumed in this lower section. The wall temperature was assumed to be 600°C at a location 1 foot above the conical section, and it linearly decreased to 200°C at the bottom of the reactor.
6. A brine makeup inlet flow of pure water at 27°C was injected into the lower cylindrical section to establish a pool of subcritical water where salts are dissolved and separated at the bottom.
7. Gravitational forces were included because the vessel was oriented vertically with the inlet flows injected downward.

Fluid properties

The physical properties (C_p, μ, k, and ρ) of the five chemical compounds (isopropyl alcohol, oxygen, nitrogen, water, and carbon dioxide) at 234.4 bar were obtained from using ASPEN PLUS, which is a chemical process simulation computer software package (ASPEN PLUS, 1994). For instance, ASPEN PLUS uses the NBS steam table (Haar et al., 1984) for the density and specific heat of water. At the critical temperature of 374°C, the specific heat is based on experimental data (Sirota and Mal'tsev, 1962). Other properties are estimated using the cubic equation of state of Schwartzentruber and Renon (1989), an extended form of the Redlich–Kwong (1979) cubic equation of state, which is recommended for highly nonideal systems at high pressure and temperature:

$$P = \frac{RT}{V + c - b} - \frac{a}{(V + c)(V + c + b)}, \quad (14)$$

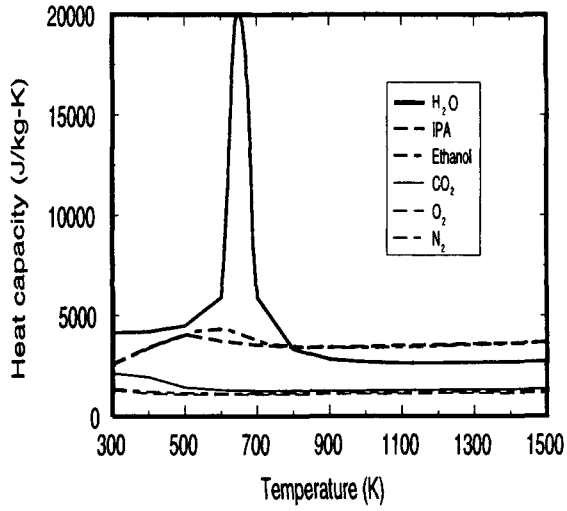

Figure 2. Heat capacities of SCWO fluids.

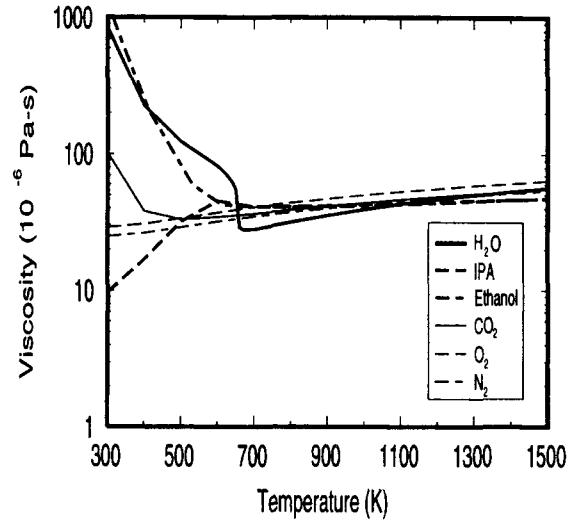

Figure 4. Viscosities of SCWO fluids.

where a is an attractive term, b is a repulsive term, and c is a volume translation term to adjust for critical properties. These binary parameters and mixing rules are built into ASPEN PLUS and estimated using the UNIFAC model (Fredenslund et al., 1975), a functional group contribution method.

Figures 2 to 5 show the specific heat, density, viscosity, and thermal conductivity of all the chemical species calculated from the equations of state just described and used in this study. As shown in these figures, the water properties changed very significantly near the critical condition of water. Figure 6 shows specific heats of water at 231 bar and near the critical temperature of 374°C from the NBS steam table and the approximation used in this study. As shown in Figure 6, the experimental values of specific heat measured by Sirota and Mal'tsev (1962) and implemented in the NBS table have a sharp curve near the critical temperature, which can result in numerical instabilities when the enthalpy equation is integrated. The approximate curve was computed to ensure that the integral of the curve was the same as that from the NBS curve so that temperatures in the flow domain of the reactor are calculated accurately. The mixture properties were computed based on mass fractions. These are ideal mixing assumptions and may not be strictly accurate at these supercritical conditions.

Chemical reaction rate

The reaction considered in this simulation was the single-step oxidation of isopropyl alcohol (IPA) given by

$$C_3H_7OH + \frac{9}{2}O_2 \rightarrow 3CO_2 + 4H_2O. \qquad (15)$$

The Arrhenius reaction rate used to model the kinetics controlled case is

$$R_{IPA} = -\frac{d[C_3H_7OH]}{dt} = a \cdot \exp\left(\frac{b}{T}\right)[C_3H_7OH], \qquad (16)$$

where

$$a = 6.801 \times 10^5 \text{ s}^{-1} \quad \text{and} \quad b = -8.126 \times 10^7 \text{ K}.$$

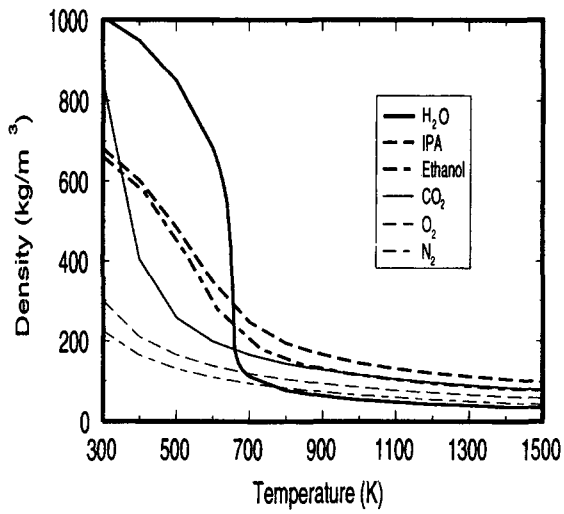

Figure 3. Densities of SCWO fluids.

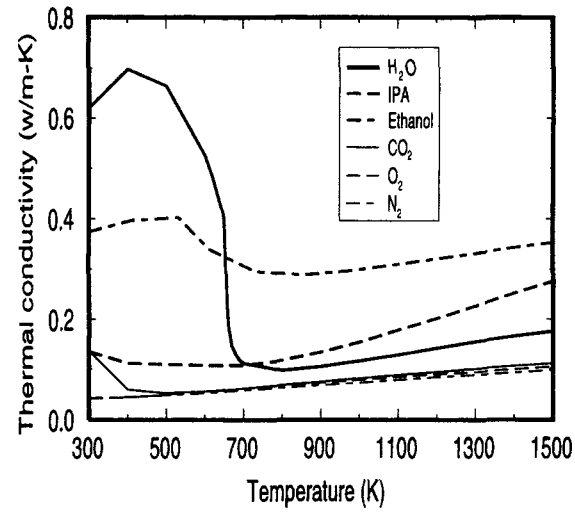

Figure 5. Thermal conductivities of SCWO fluids.

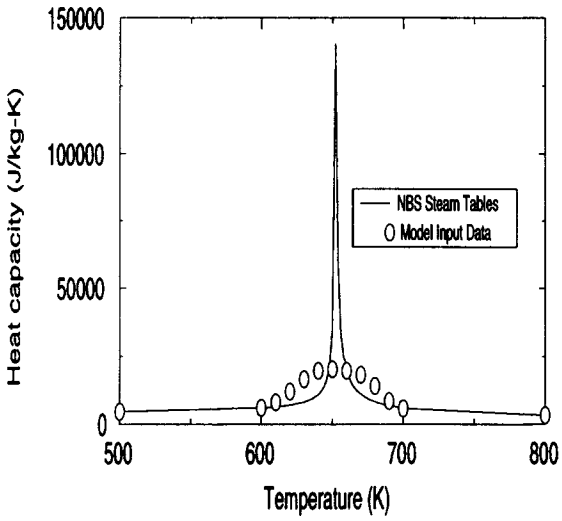

Figure 6. Comparison of actual water heat capacity at 23.4 MPa with the approximation used in the model.

There is no kinetic rate for IPA oxidation in the literature. The Arrhenius kinetic rate constants for this study were provided by MODAR. These data were regressed from non-isothermal pipe reactor temperature data, where a 25°C IPA/water stream was mixed and reacted with a 550°C water/air stream.

From our previous bench scale validation study (Oh, 1996), kinetic data from similar ethyl alcohol rate data obtained from MODAR and regressed to obtain an Arrhenius rate expression were compared with those measured by Helling and Tester (1988). The rates agreed very well at 600°C, but the MODAR data were 4–5 orders of magnitude higher at near-critical conditions. These findings led us to investigate the effect of various kinetic rates on the CFD calculations.

In order to quantify the effect of kinetic rates on the destruction efficiency and other parameters investigated, a sensitivity analysis was performed for four different rate equations. Basically, we changed the base-line isopropyl alcohol kinetic rate MODAR provided to us to account for an uncertainty band on the reaction rates.

The following cases were considered:

Case 1. Base-line MODAR kinetic rate.

$$R_{\mathrm{IPA}} = 6.801\times10^{5}\exp\left(\frac{8.126\times10^{7}}{T}\right)[C_{\mathrm{IPA}}]. \quad (17)$$

Case 2. Increase the rate constant by a factor of 10. This Arrhenius expression produces higher reaction rates in the low-temperature mixing zone:

$$R_{\mathrm{IPA}} = 6.801\times10^{6}\exp\left(\frac{8.126\times10^{7}}{T}\right)[C_{\mathrm{IPA}}]. \quad (18)$$

Case 3. Decrease the rate constant by a factor of 10. The Arrhenius expression produces lower reaction rates in the low-temperature mixing zone:

$$R_{\mathrm{IPA}} = 6.801\times10^{4}\exp\left(\frac{8.126\times10^{7}}{T}\right)[C_{\mathrm{IPA}}]. \quad (19)$$

Case 4. Keep the rate at 600°C the same as the base-line case and the rate at 375°C equal to 10% of the base line. This Arrhenius expression produces lower reaction rates in the low-temperature mixing zone:

$$R_{\mathrm{IPA}} = 5.159\times10^{8}\exp\left(\frac{1.294\times10^{8}}{T}\right)[C_{\mathrm{IPA}}]. \quad (20)$$

The Arrhenius plots for cases 1–4 are shown graphically in Figure 7.

Adiabatic Reaction Temperature Calculation

Initial CFD simulations of the MODAR test run showed that using MODAR test data inlet conditions, such as flow rates and inlet temperatures, resulted in near-wall fluid temperatures lower than the 600°C measured, perhaps indicating that some inlet boundary conditions may not be correct. To check this, we developed a method to calculate the adiabatic reaction temperature.

The adiabatic reaction temperature is defined as the temperature that would be reached if the fuel and oxidant streams mixed and reacted adiabatically. If the heat losses from the reactor are low, as they are in this pilot-scale reactor, the steady-state well-mixed outlet temperature predicted by this model will converge to a value very near the theoretical adiabatic reaction temperature.

The energy equation in terms of conservation of the static enthalpy is defined as:

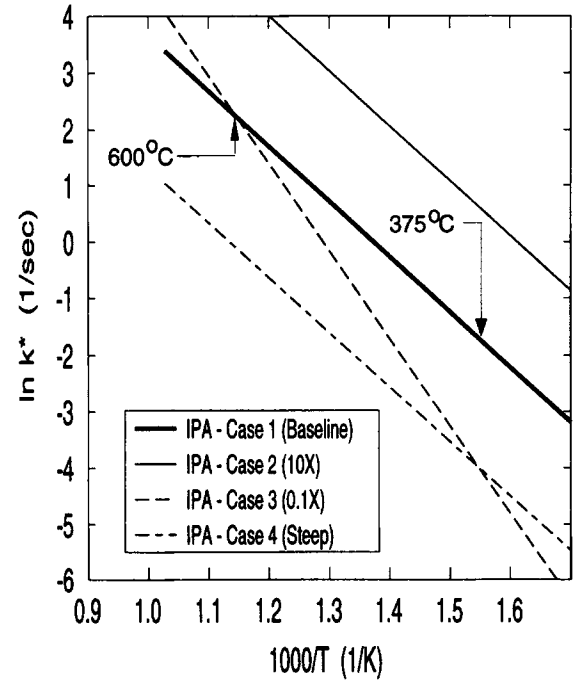

Figure 7. Variations of Arrhenius reaction-rate curves considered in this study (MODAR's IPA curve is the base line).

$$h = \sum_i m_i h_i \tag{21}$$

$$h_i = \int_{T_{\text{ref}}}^{T} c_{p,i}\, dT, \tag{22}$$

where m_i is the mass fraction, T_{ref} is a reference temperature of 27°C, and $c_{p,i}$ is the specific heat at constant pressure of species i. This sensible enthalpy does not include the enthalpy of formation of each species. For chemically reacting flows the instantaneous enthalpy, h^*, can be calculated as

$$h^* = \sum_i \left[\int_{T_{\text{ref}}}^{T} c_{p,i}\, dT + \frac{h_i^0}{M_i} + \int_{T_{\text{ref}_i}}^{T_{\text{ref}}} c_{p,i}\, dT \right], \tag{23}$$

where h_i^0 is the enthalpy of formation of species i obtained at reference temperature T_{ref_i}, and M_i is the molecular weight of species i.

The adiabatic reaction temperature is the fluid temperature that satisfies the mass-averaged enthalpy formulation and can be used as a check of input conditions. A mass-averaged instantaneous enthalpy can be expressed as

$$h^*_{\text{mixed}} = \frac{h^*_{\text{core}} \dot{m}_{\text{core}} + h^*_{\text{annulus}} \dot{m}_{\text{annulus}}}{\dot{m}_{\text{core}} + \dot{m}_{\text{annulus}}}. \tag{24}$$

Results

The results are presented in the form of temperature distribution, flow recirculation patterns, chemical reaction rates, and simulated turbulent salt-particle trajectories. All the calculations are based on a 2-D axisymmetric coordinate system and all the figures were mirror-imaged at the axisymmetric centerline. In addition, an arbitrary L/D ratio was used to show the results more clearly and to protect MODAR confidential information on the reactor geometry and nozzle configuration.

Adiabatic reaction temperature

Figure 8 shows the results of our calculation of adiabatic reaction temperature as a function of both the core-stream water flow rate and three sets of nozzle exit temperatures. An IPA flow rate of 0.125 kg/min was used for all calculations. MODAR measured a core water flow rate of 1.18 kg/min. The calculation results in an adiabatic reaction temperature of 550–575°C as opposed to temperatures of approximate 605°C measured in the MODAR test run.

The inlet boundary conditions were adjusted to obtain calculated temperatures in the range of the MODAR temperature measurements. The main parameter that controls the reactor temperatures is the fuel/water ratio. MODAR's test run obtained was not intended for comparison with CFD validation. For instance, the inlet core temperature through the axial nozzle may be higher than MODAR's measured temperature upstream of the nozzle. The nozzle is inserted into the flow domain, resulting in heat transfer through the nozzle wall. Therefore, the inlet temperatures of both streams were increased to include the effect of regenerative heating in the inlet nozzle and piping.

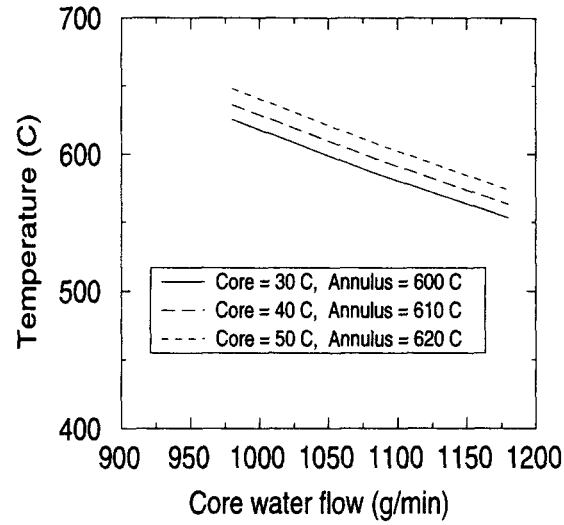

Figure 8. Calculated adiabatic reaction temperatures for 125 g/min IPA in core flow and 1,305 g/min water in annulus flow.

Using a core inlet temperature of 300°C, an annulus inlet temperature of 620°C, and a core water flow rate of 1.080 kg/min, an adiabatic reaction temperature of 609°C was predicted. The results of our analysis showed a peak reaction temperature in the reactor near 605°C and an exit temperature of 602°C.

Note that the adiabatic reaction temperature calculations depend on only the mass flows of chemical species and inlet temperatures, and the specific heats and heats of formation. Chemical kinetics affect the distribution of species and stability of reaction as discussed in a later subsection.

Fluid-temperature comparison

Using the previous adiabatic-reaction temperature calculations, we selected inlet temperatures of 600°C and 30°C for the core and annulus flows, respectively, to best match the measured temperatures.

Due to the complexity of the reactor geometry and limited instrumentation in the high-pressure system, MODAR's measured fluid temperatures are confined to temperatures near the wall. Figure 9 shows the predicted fluid-temperature distribution along the reactor vessel wall and MODAR's measured fluid temperatures at those locations. In this figure, the wall-boundary temperatures are also shown. As noted, the fluid temperatures are uniform in the upper half of the reactor outside of the reaction zone at a value of 605°C. The temperatures decrease relatively linearly as the brine pool is approached. The temperature gradient is steep near the tip of the standpipe where the temperatures are near the critical point.

As shown in Figure 9, good agreement is seen in the region of the insulated upper region; this is partially due to the fact that the core water flow and inlet temperatures were adjusted to match the calculated fluid temperatures with measured temperatures. In the lower uninsulated section where the conical region is located, the agreement is not as good. It appears as though the wall temperatures in the lower region

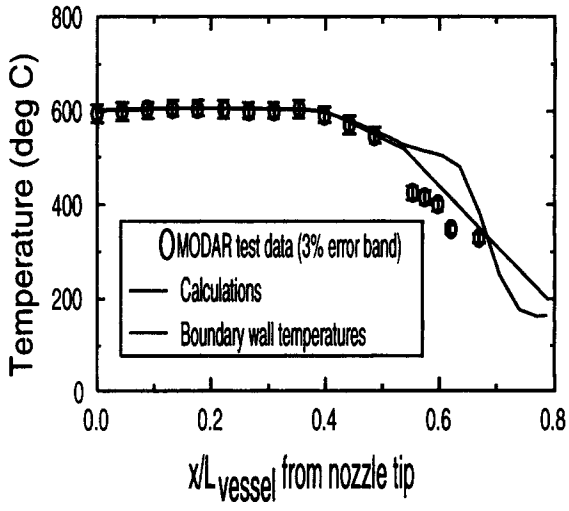

Figure 9. Comparison of MODAR near-wall test data with predicted temperatures.

are lower than the boundary conditions used in this study. Temperature comparisons in the lower section can be improved by adjusting the boundary conditions and/or modeling the conduction in the relatively thick vessel wall.

Recirculation flow pattern

The feed fluids are introduced vertically downward into the reactor and the reaction products, CO_2 and water, exit at the upper portion of the reactor. This flow configuration gives the recirculation flow pattern shown in Figure 10. This figure shows the large recirculation pattern caused by jet entrainment from the fluid exiting the nozzle and the reaction products exiting at the top portion of the reactor. The feed fluids are oxidized downstream of the nozzle when the exothermic heat is released by the chemical reaction initiated by the preheated air in the flow domain. The reaction products do not penetrate toward the bottom portion of the reactor because of buoyancy effects; the density of the reaction products is much less than the cold water injected at the bottom to maintain the brine pool. The recirculation flow pattern is important to the reactor performance. This flow has added heat from the reaction, and its entrainment serves to preheat the

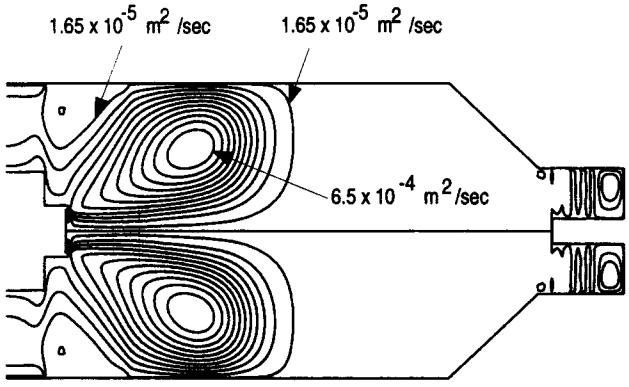

Figure 10. Predicted stream functions for MODAR run 920.

incoming feeds. The volume occupied by the recirculation causes a significant reduction in the minimum flow residence time. Also, this recirculation flow entrains small salt particles and directs them toward the nozzle tip where they can deposit due to low temperatures on the nozzle tip; this was noted by MODAR during their tests.

Effect of chemical kinetic rates

As described in the preceding section, four different chemical kinetic rates were investigated to determine the effect of Arrhenius rate constants on the sustainability of the chemical reaction. As previously discussed, the chemical kinetics does not affect the final reaction temperature as represented by the adiabatic reaction temperatures. If essentially all of the fuel is combusted, the reaction temperatures are determined by the energy input into the reactor and the effective heat capacities of the fluids. However, the rate equation does have a direct effect on the reaction distribution and, as such, has a major effect on whether a combination of flows with a given reaction temperature will sustain a stable reaction to achieve desirable destruction efficiencies.

Figure 11 shows comparison of calculated IPA reaction and mass fractions for cases 1–4. For each figure, the bottom-half side is mass fractions and the top-half side is IPA reaction rates. Mass fractions are shown in the range from 10^{-2} to 10^{-10}. The inlet mass fraction of IPA in the core nozzle is 0.1037. IPA reaction rates are shown in the peak range of -4.2 kg/m^3·s to zero outside of the reaction zone. As shown in Figure 11, the reaction zone where the chemical reaction occurs is smaller for the high reaction rate (case 2) than those for the low rate (case 3). On the other hand, the chemical reaction is delayed for the low rate and spread over a wider domain. The mass fraction is also spread out for the low rate as a result of the delayed chemical reaction. For the steep-slope case (case 4), the reaction rate was low at the low temperature, which is near the nozzle. Once the temperature reaches the operation temperature of 600°C, the reaction rate and mass fraction of IPA are nearly the same as the base case (case 1). These results indicate that the reaction flame size and mass fraction distribution depend on the reaction rate. However, IPA oxidation is achieved with more than 99.9% efficiency in the MODAR pilot-scale reactor for all reaction rates. This implies that the MODAR vessel-reactor performance is not sensitive to the specific chemical kinetic rate for a wide range of reaction parameters. This is believed to be due to the unique backmixing characteristics provided by the vessel-type reactor where the recirculation flow pattern makes the reaction-zone chemical kinetically controlled in the mixing zone and largely transport controlled outside the mixing zone as described in the following section.

Chemical kinetics/diffusion limited

Calculations were made to determine whether the reaction was either diffusion limited or kinetics limited in the reactor flow domain. For the diffusion-limited model, turbulence levels are used to calculate the reaction rate using the Magnussen and Hjertager method described in a preceding section. An Arrhenius expression is used for the kinetics-limited model. Then the values calculated from the diffusion-limited model and the kinetics-limited model are compared in each

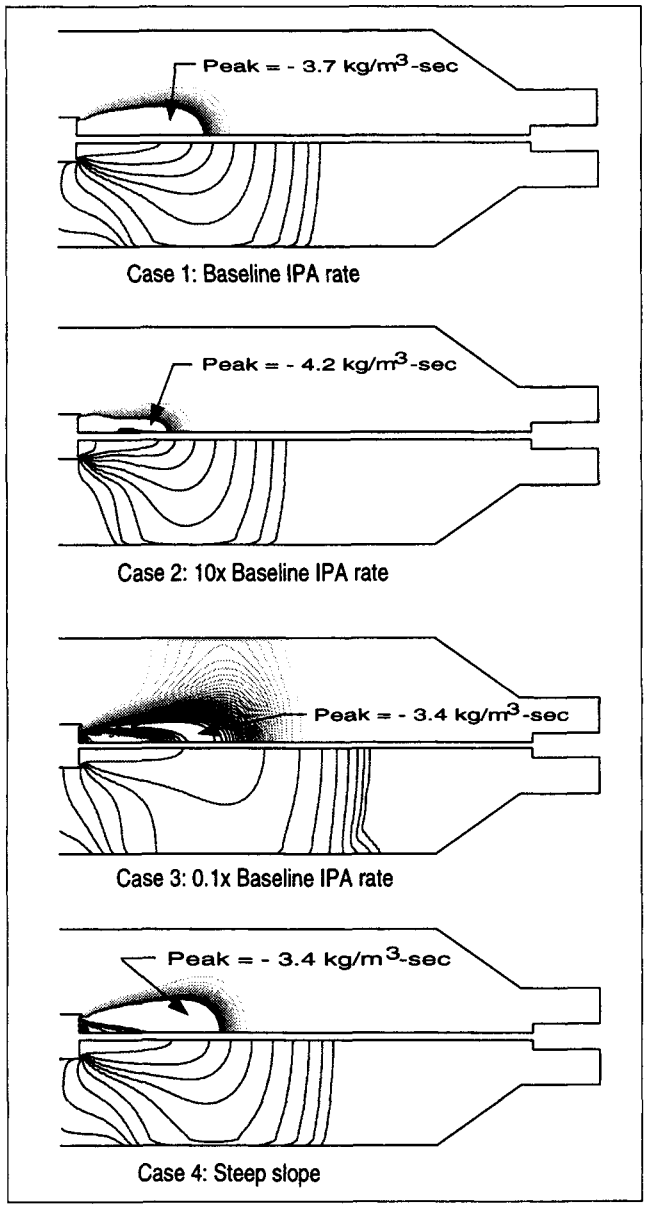

Figure 11. Comparison of IPA reaction rates and mass fractions for Cases 1–4.

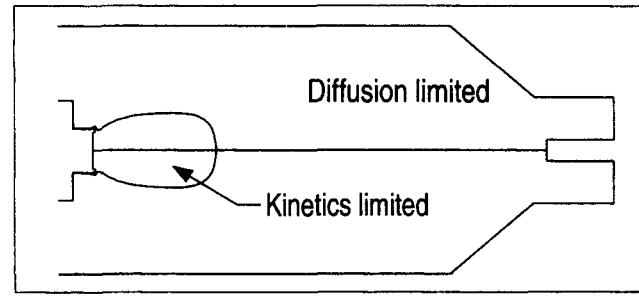

Figure 12. Boundary of kinetics/diffusion limits.

computational cell, and the smaller values of the reaction rate are taken. Figure 12 shows that the mixing zone downstream of the nozzle where the fluids are mixed and reacted is chemical-kinetics limited. Outside of this mixing zone the reaction is diffusion limited. Even though the kinetics is important in the mixing zone, the chemical reaction is initiated by the diffusion induced by flow mixing between the recirculation flow and the cold-inlet flow.

Particle trajectories

The solubility of most salts in supercritical water is very low at reaction conditions. They precipitate out in the high-temperature oxidation zone, and since they are typically sticky, they may adhere to the reactor wall upon contact. The crystallization process of salt-particle formation is not well known, but an estimate of the locations of salt-particle formation can be made. The MODAR coaxial nozzle was designed to minimize salt deposits on the wall; however, small salt particles are found to be deposited along the wall. Trajectories were calculated for two different sizes, 20 and 500 μm assuming a 50% void NaCl particle. The injection point was selected in a region where the fluid temperature is between 377–427°C, near the mixing zone between the core and annulus flows.

The flow in most of the vessel has a turbulent fluctuating velocity on the same order as the mean velocity, that is, the value of u'/U is of the order of unity. These particle trajectories were calculated from momentum, and energy balances superimposed on CFD calculated flow fields including the turbulence effect. As shown in Figure 13, there is a significant dispersion of particles. The small particles tend to be transported to the entire upper region of the reactor, while the larger ones fall to the bottom.

The results of the turbulent-flow particle-trajectory calculations are statistical in nature; plotting individual trajectories is not very helpful in analyzing the effect of different particle sizes and release points. To study the effect of particle size and release point on the turbulent trajectories, many trajectories have to be run and the particle impact points summarized. To do this, the reactor boundaries have been subdivided into several regions to receive and tabulate particle impacts. Figure 14 and Table 1 show the detailed discretization of the reactor walls and results for six particle sizes, respectively. Regions selected include the upper reactor region, the top head region, the upper, middle, and lower

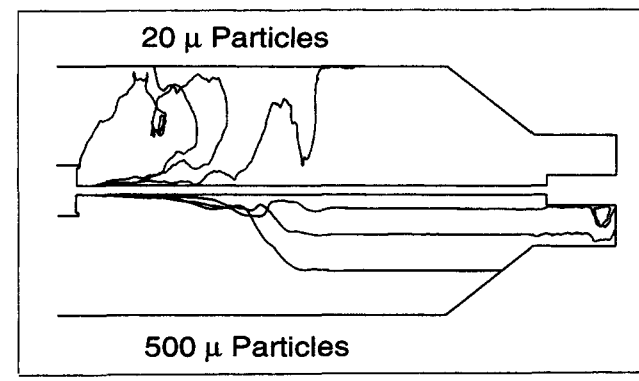

Figure 13. Typical trajectories of three 20-μ and three 500-μ particles with the effects of turbulence included.

Table 1. Wall Impact Summary for 5–1,000-μ 50% Void Salt Particles*

	5 μ r/D_{nozzle} = 0	5 μ r/D_{nozzle} = 0.3	20 μ r/D_{nozzle} = 0	20 μ r/D_{nozzle} = 0.3	100 μ r/D_{nozzle} = 0	100 μ r/D_{nozzle} = 0.3	200 μ r/D_{nozzle} = 0	200 μ r/D_{nozzle} = 0.3	500 μ r/D_{nozzle} = 0	500 μ r/D_{nozzle} = 0.3	1,000 μ r/D_{nozzle} = 0	1,000 μ r/D_{nozzle} = 0.3
W2-Outlet	3	13	5	4	0	0	0	0	0	0	0	0
W3-Top 1/3	38	34	35	36	13	23	1	3	0	0	0	0
W4-Mid 1/3	56	48	57	53	61	47	28	31	0	0	0	0
W5-Bot 1/3	3	4	2	3	0	1	1	4	0	0	0	0
W6-Cone	0	0	0	1	24	26	59	49	51	54	7	22
W7-Brine cylinder	0	0	0	0	2	2	10	7	44	42	80	68
W8-Standpipe	0	0	0	0	0	0	0	1	2	1	6	7
I4-Brine outlet	0	0	0	0	0	0	0	1	3	1	7	3
I5-Brine inlet	0	0	0	0	0	1	1	3	0	1	0	0
Aborted	0	0	1	3	0	0	2	1	0	1	0	0

*Each column represents a total of 100 injections.

thirds of the cylindrical section, the conical section, the cylindrical brine pool, and the standpipe.

Table 1 shows the results as a summary of the number of impacts (there were 100 total for each case run) for six particle sizes and two injection points. The table shows several important characteristics of the salt-particle transport. The results confirm expectations that the smaller particles are more likely to find their way to upper regions of the reactor than the larger particles. Particles less than 20 μm do not reach locations below about midpoint of the reactor, while particles greater than 500 μm do not impact higher than the conical section. Middle-size particles can impact the middle sections of the reactor. Only particles 20 μm, or smaller, reached the top head and inlet nozzle structure.

Conclusions

The current SCWO vessel reactor CFD model has evolved considerably from that used in the bench-scale study of Oh (1996). Areas of significant improvement include better fluid thermal and transport properties, a better water-specific heat approximation, addition of heat transfer to the surroundings, and inclusion of the effect of the vessel-reactor brine pool and brine takeoff. The calculations of adiabatic reaction temperatures have proven to be invaluable in establishing the sensitivities of changes in inlet conditions temperatures on reactor temperature before a full simulation is made.

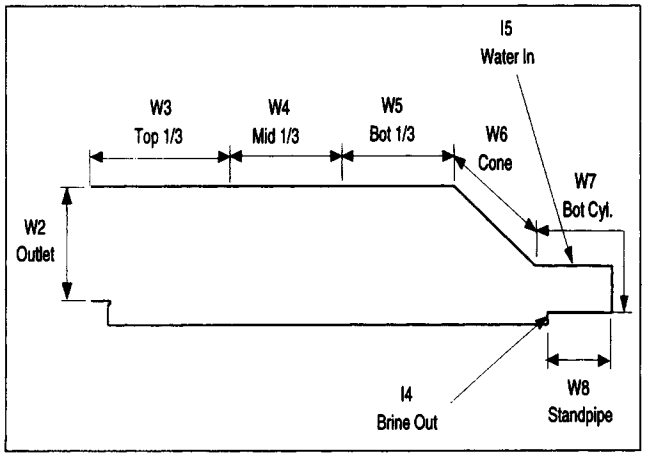

Figure 14. Salt-particle impact zones to study the effect of turbulent flow on particle transport.

The predicted temperatures of the near-wall fluid (these are the only measurements available for comparison) compare reasonably well with the limited data taken in this region. The temperature at the conical section can be improved by placing boundary conditions at those locations. Since experimental wall temperatures were not available, liner temperature gradients were used in this study, and they proved to be higher than what they should be.

The sensitivity study of the chemical kinetics indicates that the overall reactor performance is not sensitive to the kinetics, mainly because of the unique backmixing characteristics of the MODAR vessel reactor. For the low kinetic rates, the chemical reaction is delayed in the downward mixing zone while achieving the same destruction efficiencies as higher rates. This cannot be achieved in other types of SCWO reactors such as a tubular reactor. Since the vessel reactor has a fairly large radial cross-sectional area compared to a tubular- or pipe-type reactor, the limiting reaction rate is important. This study indicates that the mixing zone is kinetics-limited, while outside of the mixing zone the reaction is diffusion-limited.

The salt-particle trajectories can provide an important insight to the reactor concept in terms of a better nozzle and reactor design and optimization. Even though MODAR does not have detailed salt deposit data at the level of the detailed discretization implemented in our model, the prediction agrees qualitatively well with MODAR's findings and experience. MODAR has observed salt deposition in the upper reactor walls and the nozzle tip. Our calculations show that this is due to the entrainment of the smaller particles in the recirculating effluent. The larger particles are much easier to remove, since they tend to be transported into the cold brine pool.

In summary, this improved CFD model shows great promise in calculating the detailed thermal hydraulics and chemical-component distribution in the vessel reactor. We need to obtain more thermal data in the core region of the reactor to better validate the model for use in scale-up calculations and design optimization.

Acknowledgments

This work was performed under the auspices of the U.S. Department of Energy, Office of Environmental Management, Office of Technology Development, under the DOE Operations Office Contract No. DE-AC0794ID13223.

Notation

C = molar concentration of each reactant species, kmol/m^3
c_p = heat capacity in Eqs. 20 and 23, J/kg·K
j' = chemical species
R = real gas constant in Eq. 14, J/mol·K
t = time, s
U = mean velocity, m/s
u' = turbulent fluctuating velocity, m/s
u_1 = axial velocity, m/s
u_2 = radial velocity, m/s
V = volume in Eq. 14, m^3

Subscripts

annulus = outer annulus of the nozzle
core = inner annulus of the nozzle

Operators

$\partial/\partial t$ = partial derivative with respect to time
$\partial/\partial x_i$ = spatial derivative in the ith coordinate
D/Dt = substantial time derivative

Miscellaneous

$\min(p,q)$ = the lesser of the arguments p and q

Literature Cited

ASPEN PLUS, *ASPEN PLUS Reference Manual*, Release 9, Cambridge, MA (1994).

Barner, H. E., C. Y. Huang, T. Johnson, G. Jacobs, and M. A. Martch, "Supercritical Water Oxidation: An Emerging Technology," *J. Hazard. Mater.*, **31**, 1 (1992).

Brennecke, J. F., and C. A. Eckert, "Phase Equilibria for Supercritical Fluid Process Design," *AIChE J.*, **35**, 1409 (1989).

Buelow, S. J., R. B. Dyer, C. K. Rofer, J. H. Atencio, and J. D. Wander, "Destruction of Propellant Components in Supercritical Water," Los Alamos National Lab. Rep. LA-UR-90-1338 (1990).

Cummings, P. T., and A. A. Chialvo, "Molecular Simulation Study of Solvation Structure in Supercritical Aqueous Solutions," *Chem. Eng. Sci.*, **49**(17), 2735 (1994).

Dixon, C. N., and M. A. Abraham, "Conversion of Methane to Methanol by Catalytic Supercritical Water Oxidation," *J. Supercrit. Fluids*, **5**, 4 (1992).

Fluent Inc., *FLUENT User's Manual*, Version 4.4, Lebanon, NH (1996).

Fredenslund, A., R. L. Jones, and J. M. Prausnitz, *AIChE J.*, **21**, 1086 (1975).

Gloyna, E. F., "Supercritical Water Oxidation-Deep-Well Technology for Toxic Wastewaters and Sludges," Univ. of Texas Rep. W-89-1 (1989).

Haar, L., J. S. Gallagher, and G. S. Kell, *NBS/NRC Steam Tables*, Hemisphere Publishing Corporation, New York (1984).

Helling, R. K., and J. W. Tester, "Oxidation of Simple Compounds and Mixtures in Supercritical Water: Carbon Monoxide, Ammonia, and Ethanol," *Environ. Sci. Technol.*, **22**, 11 (1988).

Hong, G. T., "Hydrothermal Oxidation: Pilot Scale Operating Experiences," Water Conf., Pittsburgh (1995).

Johnston, K. P., and C. Haynes, "Extreme Solvent Effects on Reaction Rate Constants at Supercritical Fluids Conditions," *AIChE J.*, **33**, 2017 (1987).

Killilea, W. R., K. C. Swallow, and G. T. Hong, "The Fate of Nitrogen in Supercritical Water Oxidation," *J. Supercrit. Fluids*, **5**, 72 (1992).

Klein, M. T., L. A. Torry, B. C. Wu, and S. H. Townsend, "Hydrolysis in Supercritical Water: Solvent Effects as a Probe of the Reaction Mechanism," *J. Supercrit. Fluids*, **3**, 222 (1990).

Kochan, R. J, and C. H. Oh, "CFD Model Development and Data Comparison for Thermal-Hydraulic Analysis of HTO Pilot Scale Reactor," Idaho National Engineering Lab. Rep. INEL-95/0445 (1995).

McBrayer, R. N., and J. W. Griffith, "Operation of the First Supercritical Water Oxidation Industrial Waste Facility," Int. Water Conf, Pittsburgh, p. 52 (1995).

Magnussen, B. F., and B. H. Hjertager, "On Mathematical Models of Turbulent Combustion with Special Emphasis on Soot Formation and Combustion," Symp. on Combustion, Cambridge, MA (1976).

Marshall, W. L., and E. U. Frank, "Ion Product of Water Substance, 0–1,000°C, 1–10,000 bar, New International Formulation and Its Background," *J. Phys. Chem. Ref. Data*, **10**(2), 295 (1981).

Modell, M., *Standard Handbook of Hazardous Waste Treatment and Disposal*, Sec.8.11, H. M. Freeman, ed., McGraw-Hill, New York (1989).

Modell, M., "Processing Methods for the Oxidation of Organics in Supercritical Water," U.S. Patent No. 4,543,190 (1985).

Moore, R. C., and J. M. Simonson, "A Review of Supercritical Water Oxidation Research and Technology," Oak Ridge Nat. Lab. Rep. ORNL/CF-93/39 (1993).

Morsi, S. A., and A. J. Alexander, "An Investigation of Particle Trajectories in Two-Phase Flow Systems," *J. Fluid Mech.*, **55**(pt. 2), 193 (1972).

Oh, C. H., and R. J. Kochan, "Modeling of Thermal Characteristics in Supercritical Water Oxidation Reactors," Int. Workshop on Supercritical Water Oxidation, Amelia Island, FL (1995).

Oh, C. H., and R. J. Kochan, "Thermal-Hydraulic Modeling of Supercritical Water Oxidation of Ethanol," *Energy & Fuels*, **10**(2), 326 (1996).

Orszag, S. A., V. Yakhot, W. S. Flannery, F. Choudhury, D. Maruzewski J., and B. Patel, *Near Wall Turbulent Flows*, Elsevier, New York, p. 1031 (1993).

Patankar, S. V., *Numerical Heat Transfer and Fluid Flow*, Hemisphere, Washington, DC (1980).

Redlich, O., and J. N. S. Kwong, "On the Thermodynamics of Solutions: V. An Equation of State, Fugacities of Gaseous Solutions," *Chem. Rev.*, **44**, 223 (1979).

Rice, S. F., R. R. Steeper, and C. A. LaJeunesse, "Destruction of Representative Navy Wastes Using Supercritical Water Oxidation," Sandia National Lab. Rep. SAND94-8203 (1993).

Savage, P. E., S. Goplan, T. I. Mizan, C. J. Martino, and E. E. Brock, "Reactions at Supercritical Conditions: Applications and Fundamental," *AIChE J.*, **41**, 7 (1995).

Savage, P. E., and M. A. Smith, "Kinetics of Acetic Acid Oxidation in Supercritical Water," *Environ. Sci. Technol.*, **29**, 216 (1995).

Schwartzentruber, J., and H. Renon, "Extension of UNIFAC to High Pressures and Temperatures by the Use of a Cubic Equation of State," *Ind. Eng. Res.*, **28**, 1049 (1989).

Sirota, A. M., and B. K. Mal'tsev, *Teploenergetika*, **9**(1), 52 (1962).

Tester, J. W., P. A. Webly, and H. R. Holgate, "Revised Global Kinetics Measurements of Methanol Oxidation in Supercritical Water," *Ind. Eng. Chem. Res.*, **32**, 236 (1992).

Tester, J. W., H. R. Holgate, F. J. Armellini, P. A. Webly, W. R. Killilea, G. T. Hong, and H. E. Barner, "Supercritical Water Oxidation Technology: Review of Process Development and Fundamental Research," *Emerging Technologies in Hazardous Waste Management III*, *ACS Symp. Ser.*, 518, p. 35 (1993).

Uematsu, M., and E. U. Frank, "Static Dielectric Constant of Water and Steam," *J. Phys. Chem. Ref. Data*, **9**(4), 1291 (1980).

Yakhot, V., and S. A. Orszag, "Renormalization Group Analysis of Turbulence: I. Basic Theory," *J. Sci. Comput.*, **1**(1), 3 (1986).

Manuscript received Oct. 15, 1996, and revision received Feb. 6, 1997.